Nano Research

ISSN 1998-0124 CN 11-5974/O4
https://doi.org/10.1007/s12274-019-2295-x

Research Article

# High-pressure triggered quantum tunneling tuning through classical percolation in a single nanowire of a binary composite

HPSTAR 699-2018

Sudeshna Samanta[1,2], Mokwon Lee[3], Deok-Soo Kim[3], Jaeyong Kim[2], and Lin Wang[1] (✉)

[1] *Center for High Pressure Science & Technology Advanced Research, Shanghai 201203, China*
[2] *HYU-HPSTAR-CIS High Pressure Research Center, Department of Physics, Hanyang University, Seoul 04763, Republic of Korea*
[3] *Voronoi Diagram Research Center, School of Mechanical Engineering, Hanyang University, Seoul 04763, Republic of Korea*



**Received:** 13 November 2018 / **Revised:** 24 December 2018 / **Accepted:** 3 January 2019

## ABSTRACT

In the era of miniaturization, the one-dimensional nanostructures presented numerous possibilities to realize operational nanosensors and devices by tuning their electrical transport properties. Upon size reduction, the physical properties of materials become extremely challenging to characterize and understand due to the complex interplay among structures, surface properties, strain effects, distribution of grains, and their internal coupling mechanism. In this report, we demonstrate the fabrication of a single metal-carbon composite nanowire inside a diamond-anvil-cell and examine the *in situ* pressure-driven electrical transport properties. The nanowire manifests a rapid and reversible pressure dependence of the strong nonlinear electrical conductivity with significant zero-bias differential conduction revealing a quantum tunneling dominant carrier transport mechanism. We fully rationalize our observations on the basis of a metal-carbon framework in a highly compressed nanowire corroborating a quantum-tunneling boundary, in addition to a classical percolation boundary that exists beyond the percolation threshold. The structural phase progressions were monitored to evidence the pressure-induced shape reconstruction of the metallic grains and modification of their intergrain interactions for successful explanation of the electrical transport behavior. The pronounced sensitivity of electrical conductivity to an external pressure stimulus provides a rationale to design low-dimensional advanced pressure sensing devices.

## KEYWORDS

single metal-carbon nanowire, high pressure, electrical transport, Voronoi diagram

## 1 Introduction

Nanoscale structures (nanowires and nanotubes) are renowned for their pressure-induced capacitive and piezoelectric responses in flexible pressure sensors [1–5]. In contrast, resistivity has been used in limited cases for designing strain-gauge sensors [2, 6, 7]. Although they are industrially-friendly, extreme miniaturization impedes the detection of their response to external stimuli [3, 8, 9]. At a single nanowire level, the situation is even more complex and thus, it is an urgent challenge for essential physics to engineer and manipulate individual 1D nanostructures [10]. Among the numerous nanomaterials, "soft"-carbon matrix based binary composites that include "rigid"-fillers offer superior physical and mechanical properties for electronic devices [11–15]. The heterogeneous nature in the "microscopic" length scale rules the effective "macroscopic" properties and is highly tunable by the spatial arrangement of those constituents [14, 16, 17]. For example, a stimuli-induced drastic change in electrical conductivity was demonstrated for metallic nanoislands deposited on graphene attributed by the tunneling conductance at percolation threshold [15, 18–21]. Such precise compositional homogeneity often offers "on-demand" nanoscale write-read-erase [22], superconductivity [23], metal-insulator transitions [24], or electrical transport properties in quantum-metals [25, 26].

Recent works on binary composites highlight the effect of the dimension, environment, and frameworks on nanomaterials, but research rarely extends to driving forces like external hydrostatic pressure [19–21, 24–28]. A minute pressure triggers a dramatic change in the electrical resistivity when a system dimension becomes comparable to the electronic mean free path [29]. Moreover, pressure initiates an irreversible amorphous-to-crystalline phase transition, enhancement of the bulk modulus, and Debye temperature in metal nanocrystals through an energetically favorable route [16, 30]. These conditions offer advanced functionalities for 2D monolayers, self-assembled nano-superlattices, and functional nanoparticles [31, 32]. However, using external pressure to cause thermodynamic responses in a nanoscale composite device is yet to be explored, and could lead to the realization of futuristic operational pressure sensors.

Herein, we fabricated a single binary composite nanowire (metallic nanocrystalline platinum-amorphous carbon) by a nanolithographic process to study its electrical resistivity under applied pressure. The compression allowed high electrical conductivity and quantum tunneling conductance due to the significant changes in interparticle separation in the microstructures of the growing metal network. High-resolution transmission electron microscopy (HRTEM) provided more opportunities to record the microstructural response of the nanocomposite to external stimulus. Finally, our observations are rationalized with a theoretical model based on the spatial distribution of metallic fillers in the composite nanowire interior to explore the origin of its electrical conductivity.

## 2 Experimental

### 2.1 Material

Before initiating pressure-induced processes, the platinum-amorphous

Address correspondence to wanglin@hpstar.ac.cn

carbon binary nanocomposite (Pt-C) nanowires were fabricated by focused-ion-beam induced deposition (FIBID) (Fig. S1 in the Electronic Supplementary Material (ESM)). Figure 1(a) shows the morphology and structure of an as-prepared nanowire on one of the clean diamond culet surfaces. Figure 1(b) illustrates the four-probe geometry inside the diamond-anvil-cell (DAC). The qualitative and quantitative compositional analysis were recorded by *in situ* energy dispersive X-ray (EDX) (Table S1 in the ESM) during a single synchronized deposition of a nanowire (length 280 μm; width and thickness approximately 100 nm (Fig. 1(a)). The attributed morphology and crystallinity of the f.c.c platinum grains in the carbonaceous matrix were revealed by the HRTEM images shown in Fig. 1(c). Figure 1(d) shows the statistical distribution of the platinum grains with an average diameter of 2–3 nm. However, the overall characteristics are highly dependent on the surface roughness, lattice mismatch, thickness of the nanowire, and the FIBID parameters (Fig. S2 in the ESM) [33].

### 2.2 Methods

We used a commercial FEI dual-beam system (Helios 600) to fabricate FIBID Pt-C NW on one surface of our patterned diamonds procured from Almax-easyLab [33] with a culet size of 780 μm, prefabricated with four conducting gold electrodes (Fig. S1 in the ESM).

Gold contact pads in a four-probe configuration connected the nanowire and a silver-conducting epoxy attached the wires to external instruments for electrical transport measurements. An insulating gasket coated with CBN-epoxy was used. Silicone oil was used as a pressure transmitting medium (PTM) and a small ruby chip was the pressure marker. Direct current $I-V$ measurements were completed at room temperature (RT = 300 K) for $P$ (0–5 GPa with a current compliance 10 μA, current density $j \approx 10^9$ A/m$^2$ < $j_{max} \approx 10^{10}$ A/m$^2$ to avoid electromigration damage.

Cross-sectional HRTEM images were collected in a JEOL microscope equipped with Gatan spectrometer from the recovered nanowires after each compression to a particular pressure value (Fig. S3 in the ESM).

## 3 Results and discussion

### 3.1 Electrical transport under compression

Hydrostatic pressure ($P$) dependent electrical resistivity ($\rho$) was measured in a single nanowire up to $P \cong 5$ GPa using a DAC to avoid a stress-induced fracture regime, finding $P \geq 6$ GPa for the 100 nm FIBID carbon nanowire [34]. The ambient resistivity $\rho_0 =$ 3.5 μΩ·m matched well with previous reports [24, 35], however, it appeared significantly higher compared to the bulk metals [24, 36–39]. Figure 2(a) shows the pressure-dependent resistivity at 300 K (RT) with two sharp resistivity transitions at pressures $P_{c1}$ and $P_{c2}$ and three separate distinct regimes; $P_A$, $P_B$ and $P_C$. In region $P_A$, $\rho$ increased slowly with pressure and exhibited an abrupt switch with $R_{ON} / R_{OFF} \approx 20$ around 0.9–1.1 GPa, which is comparable with the piezoresistive response of a previously reported single Si nanowire [40]. $R_{ON}$ and $R_{OFF}$ correspond to the resistivitivities of the nanowire recorded in regions $P_B$ and $P_A$ respectively. The piezoresistance effect in Si nanowire was highly coupled to its electrical conductivity and mechanical manipulation. Under compression, the relative change of its conductivity was as high as 15 compared to 0.08 for bulk Si. Such giant piezoresistance effect was nonlinear with high mobility of charge carriers and effective for strain engineering in futuristic nanoscale devices. Figure 2(b) corresponds to the relative change in resistance $\Delta\rho / \rho = \dfrac{\rho - \rho_0}{\rho}$ for $P < 3$ GPa. A strong switching behavior often induces a nonlinear response and tunneling effects, as found in piezo-resistive composites [12, 14]. The temperature ($T$)-dependent resistivity was additionally measured at ambient pressure (Fig. 2(c)). The negative temperature coefficient of resistivity confirmed that the majority phase in the nanowire was an insulating a-C phase (upper inset Fig. 2(c)) [24, 35, 41].

To elucidate the abrupt change in resistivity at low pressures, the thickness ($t$) dependent resistivity for FIBID nanowires is plotted in Fig. 2(d) at ambient conditions [24, 35, 36, 42, 43]. First, it decreases abruptly with an increase of thickness and then changes slowly for $t \geq 100$–$200$ nm [41]. The critical thickness $t_{crit}$ is reported as 50 nm or even lower [24, 42]. Mott's maximum resistivity ( $\rho^{Mott}|_{max} \sim$ 30 μΩ·m) for the metallic conduction (a crossed pentagon in Fig. 2(a) and a dashed line in Fig. 2(d)) separates two distinct electrical conductivity regimes around $t_{crit}$. A large deviation in the absolute resistance ($R$) as a function of the ratio of nanowires' physical dimension ($l/A$) also demonstrates a critical dimension as shown in Fig. 2(d) (inset) ($l$ and $A$ are the nanowire length and an area of cross-section) [29, 42]. The resistivity values of the nanowire under pressure were compared, and we postulate that the nanowire might reduce its thickness during compression, where a sharp rise in resistivity could be expected.

The nanowire possessed a widely different bulk-modulus $B_{Pt-C} = 18 \pm 3$ GPa and thermal expansion coefficient than diamond ($B_D$) (in the ESM) [16, 44]. $B_D \gg B_{Pt-C}$ causes extreme anisotropy in the elastic-moduli depending on its geometry [45]. The substrate-mediated biaxial strain ($\epsilon_D = P / B_D$) can be transmitted through the nanowire with an efficiency α and $\epsilon_{NW} = \alpha\epsilon_D$. Thus, the biaxial stress on the nanowire is $\sigma_{NW} = \alpha(\sigma_{NW})\dfrac{\beta_{NW}}{B_D}P$, where $\beta_{NW}$ is Young's modulus and $\alpha$ may vary with stress. By considering a simple stacking of the PTM-nanowire-diamond as shows in Fig. 2(e) and assuming full efficiency in the pressure transfer, the result is $\alpha = 1$. Practically, $\alpha$ varies with surface roughness and adhesion in the diamond-nanowire interface mediating the slipping process, buckling, and defect creation [46]. The absence of any physical slipping of the nanowire from the diamond culet does not rule out the possibility of creating a local inhomogeneous stress-strain field. A partial strain transfer ($\alpha < 1$) from diamond to nanowire (amorphous-crystalline interface) is expected and is analogous to the graphene-$SiO_2$ interface with $\alpha = 0.2 \pm 0.1$ [46]. Hence, apart from the high conformation of nanowire on diamond, poor adhesion might lead to a critical biaxial

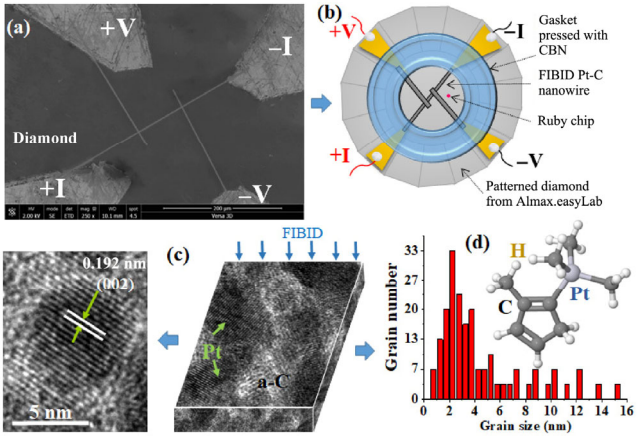


**Figure 1** (a) Scanning electron microscopy (SEM) image of a single Pt-C nanowire on a diamond culet surface. (b) Four-probe geometry for electrical transport measurement inside the DAC. (c) HRTEM images at ambient conditions confirm metallic platinum grains in amorphous carbonaceous matrix. A single platinum nanograin with atomic plane spacing 0.192 nm (002) confirms fcc lattice. (d) Statistical distribution of the grain-size of the as deposited sample. Inset: molecular model of the precursor gas in FIB (built by Jmol).

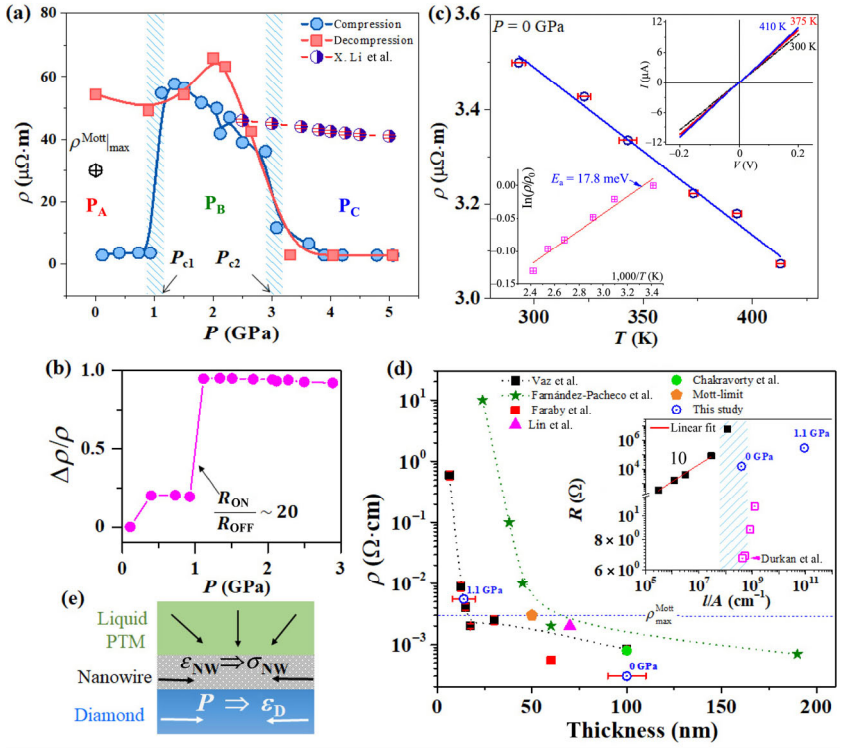


**Figure 2** (a) The variation of $\rho$ with the $P$ on nanowire compared with the a-C [52]. (b) Pressure-induced change in $\Delta\rho/\rho$ shows $R_{ON}/R_{OFF} \sim 20$. (c) $\rho - T$ data of the nanowire at ambient pressure with $ln(\rho/\rho_0)$ versus 1,000/$T$ at few representative $I$–$V$ characteristics (inset). (d) The variation of resistivity with the thickness of various nanowires. Inset: modification in $R$ with $l/A$. (e) PTM-nanowire-diamond stacking inside a DAC (see text).

strain $\sigma_{NW}^{Crit}$ corresponding to a certain pressure incorporating the partial unbinding process [45, 47, 48]. Locally strained regions can develop interesting percolation and tunneling phenomena as recently observed in a nanogragular tunneling resistor [49]. $P_{c1}$ might correspond to a $\sigma_{NW}^{Crit}$ where the nanowire stabilizes under the biaxial strain field. In addition, the a-C matrix undergoes an amorphous-amorphous phase transition around 0.75 GPa [44]. A transition from sp$^2$-rich to sp$^3$-rich a-C under biaxial stress resulted in a sharp increase of resistivity by 5 orders of magnitude [50]. The electrical resistivity of a carbon fiber polymer was enhanced by increasing the inter-electronic distances at dangling-bond pairs for $P >$ 0.3 GPa [51]. The excess dangling bonds later caused an irreversible change of resistivity that might resemble the transition around $P_{c1}$ (Fig. 1(a)) (decompression).

In the $P_B$ region, resistivity decreased faster with increasing $P\left(\frac{d\ln\rho}{d\ln P} = -0.26\ \text{GPa}^{-1}\right)$ than the earlier observation (–0.039 GPa$^{-1}$) in a-C [52]. Writing pressure dependencies of $\rho$ as $\frac{d\ln\rho}{dP} = \frac{d\ln(n_C)}{dP} + \frac{d\ln\mu}{dP}$ ($n_C$ and $\mu$ are the density and mobility of the charge carriers, respectively), estimated $n_C \approx 10^{20}$/cm$^3$ with $\mu = 10$ cm$^2$/Vs at RT [53]. The system appeared to be a quasi-intrinsic semiconductor in $P_B$ followed by a reversible transition at $P_{c2}$ during decompression.

We recorded the pressure-dependent four-probe current-voltage ($I - V$) characteristics in three distinct regions. The $I - V$ curves were linear in regions $P_A$ and $P_C$, as depicted in Figs. 3(a) (0.7 GPa) and 3(b) (4.8 GPa), respectively. The behavior differed dramatically in the $P_B$ region and a non-linear behavior with two different current-voltage dependencies were clearly visible in Fig. 3(c) ($P \sim$ 2.3 GPa). Figure 3(d) shows that for low (high) applied voltages, the current increased linearly (exponentially). At low-bias, the slope $S_1 \sim 1.029$ (±0.005) suggests the charge carriers are trapped across

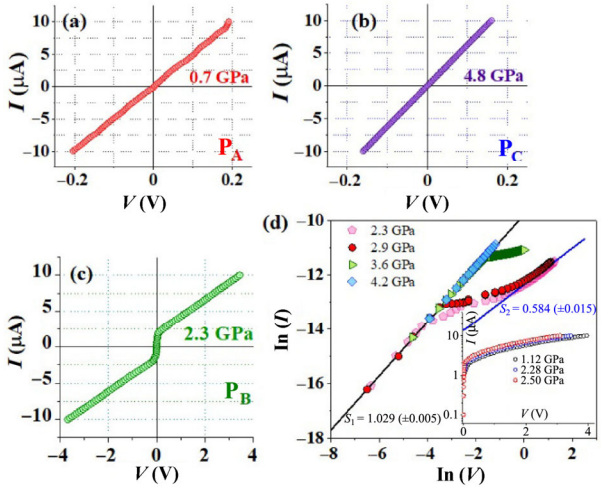


**Figure 3** (a)–(c) $I - V$ characteristics (compression) of the nanowire at three representative pressure values. (d) A crossover from $I \propto E^{S_1}$ to $I \propto \exp(V^{S_2})$ from low-bias to high-bias voltages (solid lines) shows highly nonlinear current-voltage dependencies with pressure (inset).

the metallic grains and at the grain boundaries. A transition from $S_1 \sim 1$ (linear dependency) to a slope $S_2 \sim 1/2$ (square-root dependency) indicates the emergence of longer intertrap distances during compression. At higher voltages, the nonequilibrium population of the trap states might give rise to the non-uniform electric field distribution along the length of compressed nanowire, which is in fair agreement with the data in Fig. 1(c). Finally, we note that, if the thickness of the nanowire is comparable to the intertrap distances, the alternative conduction mechanisms such as direct tunneling and trap-assisted tunneling might become significant.

### 3.2 Pressure-induced percolation and tunneling mechanism

Altogether, the above results are best described in terms of

pressure-induced percolation and tunneling conduction with a binary component model. The metallic grains can be identified by their diameter $D$ with its volume part $0 \le v \le 1$ (spherical grains) along with the critical $v_c$ corresponding to a percolation threshold. At $P_{th} = 2.9$ GPa, we estimated $v_c \approx 0.31$ using $\rho - P$ data and the Murnaghan equation of state (EOS) of a-C (in the ESM) [44]. The solid lines in Fig. 4(a) show fits for the scaling laws as follows: $\rho \propto (v_c - v)^m$ and $\rho \propto (v - v_c)^{-n}$ for the insulating and metallic regimes, respectively. Interestingly, our experimental $P_{th}$ matched very well with the calculated $P_{th}^{perc} = 2.7$ GPa from percolation theory and thus, validates the applicability of our model fits. Figure 4(b) shows the estimated energy with the volume. The estimated metallic grains in a volume unit are $\eta = (2v / D^3)$ and the average distance between the grains is $r_g = D(2 / v)^{1/3}$. Finally, we identified the increase of conductivity after a certain pressure at $P_{c2}$ as a result of percolation among the platinum grains.

Differential conductance $G(= \mathrm{d}I / \mathrm{d}V)$ and its derivative $\mathrm{d}G / \mathrm{d}V$ both highlight strong pressure sensitivity. For low-bias voltages $-0.5\ \mathrm{V} \le V \le 0.5\ \mathrm{V}$, Fig. 4(c) shows that $G$ exhibited a strong zero-bias-conductance-hump (ZBCH) signifying a tunneling conduction mechanism (Fig. S4 in the ESM). FIBID binary composites are often regarded as disordered electronic materials where the inter-grain surface scattering and interactions are crucial [26, 36, 38, 43]. An important intragrain energy scale can be defined as $\Delta = 1 / [N(\epsilon_F)V_0] \sim \epsilon_F / (kr)^3$ where $N(\varepsilon_F) \propto m^{3/2}\varepsilon_F^{1/2} / h^3$ and $V_0 (\propto r^3)$ are the density of states at the Fermi level and the volume of the grain ($r$: grain radius), respectively [24, 39, 54, 55]. At room temperature, platinum's Fermi level $\epsilon_F = 9.74$ eV estimates $r^3 = 3.7 \times 10^{-27}$ m$^3$ and $r \sim 1.6$ nm, which is highly consistent with our experimental grain size ~2 nm (Fig. 1(d)) with an estimation of electron energy quantization.

Figure 4(d) shows the normalized differential conductance $G / G_0$ along with $\dfrac{\mathrm{d}G}{\mathrm{d}V} = \dfrac{\mathrm{d}^2 I}{\mathrm{d}V^2}$ at 2.9 GPa to emphasize the oscillations observed in $\mathrm{d}G / \mathrm{d}V$. Figure 4(e) schematically shows the tunneling mechanism in the adjacent grains. Similar ZBCHs were found earlier in thin Pt-C ($t < 50$ nm) nanowires, gold atomic wires, and single-walled carbon nanotubes [3, 24, 56, 57]. At RT and under compression, the calculated electron mean free path is $l_e \approx 10^{-11}$ m $<< l_p$ (phase coherence length), or the dimension of the nanowire. Hence, phase-incoherent and phase-randomized charge carriers along

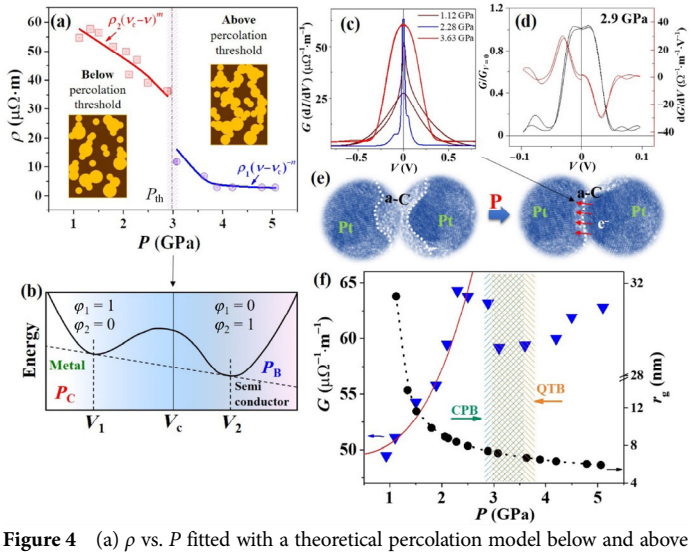


**Figure 4** (a) $\rho$ vs. $P$ fitted with a theoretical percolation model below and above $P_{th}$. (b) Schematic of the expected energy as a function of volume. (c) Variation of the $G$ with $P$ and (d) the broadening of $G / G_{V=0}$ along with the oscillations in $\mathrm{d}G / \mathrm{d}V$ at $P_{th}$. (e) External pressure induced tunneling mechanism between the metallic grains. (f) $G$ varies with $P^\gamma$ (solid line) below CPB and remained unchanged above the QTB (see text). The right axis shows the variation of $r_g$ with $P$.

with the finite potential barriers at electrode-nanowire interfaces could give asymmetries and oscillations in conductance.

A tight-binding Hamiltonian deduced the competition and relationship between tunneling with localization around $P_{th}$ [54], introducing three distinct conductivity regions: (i) a classically localized (CL) phase (electrons scatter from the disorders); (ii) a quantum liquid (QL) region (tunneling dominated and the localization effect is suppressed); and (iii) an extended metallic (EM) phase (weak localization). The CL phase closely resembles the pressure region 1–2.3 GPa in our case and the QL region set in just after it, when the tunneling was sufficiently strong. The quantum particles cannot propagate before they reach the classical percolation threshold [54]. The survival of tunneling conduction just above $P_{th}$ strongly supports the existence of the QL region. Figure 4(e) schematically displays the tunneling mechanism between adjacent metallic nanograins. Figure 4(f) shows that $G$ increased sharply as $G \propto P^\gamma$ ($\gamma = 2.9$) below $P_{th}$, below the classical percolation boundary (CPB). Above the QL boundary (QTB), the system enters into an EM phase. The region sandwiched between the CPB and QTB was highly inhomogeneous with strong tunneling conductance. We believe that the pressure-induced conduction process handed over from a percolation to a percolation-assisted tunneling in the Pt-C nanowire. $r_g$ also decreased drastically around $P_{th}$, as shown in the right axis in Fig. 4(f). Although pressure favored overlapping, merging, and shape reconstruction of metallic grains, any mechanical failure (compression damage) or blowing (current damage) of the nanowire was absent after the completion of experiments (Fig. S5 in the ESM).

### 3.3 Microstructural evolution under compression

We explored the pressure-induced microstructural evolution with a series of cross-sectional HRTEM analysis, as illustrated in Fig. 5 (left panel). Ambient pressure HRTEM was considered the standard. Images of the recovered samples were collected by keeping identical FIBID parameters and performing the hydrostatic compression on several nanowires. The fcc cubic polycrystalline platinum grains can be easily identified with planer distances (atomic planes) of 0.2277 nm (111), 0.1972 nm (002), 0.1394 nm (022), and 0.1138 nm (222) with a lattice parameter of 0.3924 nm. For bulk platinum, (111) corresponds to 0.2265 nm, which confirms that the FIBID material did not suffer any residual strain during deposition [30]. For $P \approx 0.7$ GPa, the isolated platinum grains moved closer and the necessary energy was supplied by the external pressure. Around $P_{th}$, an interesting feature is the existence of bottlenecks constituting bridges between the two metal grains. A typical representation of the bridge formation (dashed line for 2.9 GPa) between the adjacent grains is shown in Fig. 5(c). Upon further compression, the platinum grains coalesced together and bigger grains became more distinct. The atomic diffusion process could be an energetically favorable mechanism to relax the strain in the sample, resulting in the nanoscale grain growth (~ 15 nm at 5.6 GPa) [30]. It is evident that the individual platinum grain overlapped and became indistinguishable, allowing the current to find the shortest path resulting in high conductivity in a continuum percolating metal network.

We introduced Voronoi network simulation modelling (in the ESM) to simulate the conduction mechanism corresponding to the HRTEM results, as shown in Fig. 5 (right panel) (yellow area: platinum nanograins, indigo lines: equidistant points between two neighboring metallic grains). Voronoi network simulation was introduced for this purpose to extract the geometric features like area, boundary length, diameter of platinum grains from HRTEM images. Both theoretical and practical applications pursue evidence for the remarkable conductivity changes in nanowire through microscopic modifications in the binary composite [58]. With these topological information, the modelling calculates the number of adjacent grains or the shortest distance between two neighboring grains. At ambient, both experiment and simulation results can identify

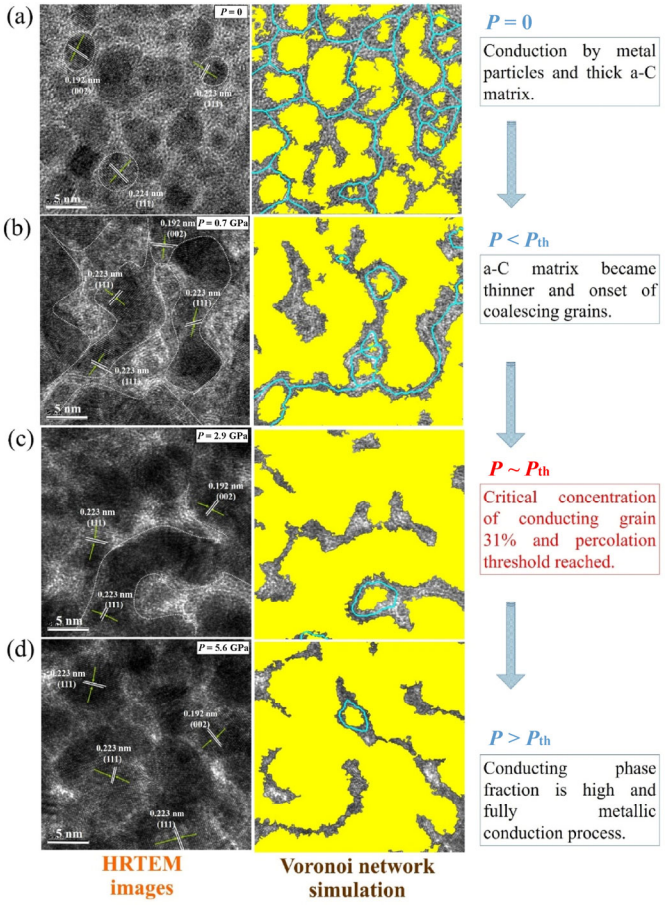


**Figure 5** Left panel: Cross-sectional HRTEM images of recovered nanowires at (a) ambient, (b) 0.7 GPa, (c) 2.9 GPa, and (d) 5.6 GPa. The dotted line shows the formation of bottlenecks in the vicinity of $P_{th}$. Around 5–6 GPa, the metallic grains interconnected and overlapped together forming a metallic continuum. Right panel: the results from Voronoi network modelling related to the HRTEM images (yellow: the amount of irregular conducting fillers, indigo: the distinguishable boundaries).

discrete grains separated by long boundaries (solid indigo lines). For $P < P_{th}$, the grains started to grow and significant shrinkage of lengths of the boundaries was observed. The situation supported the tunneling conductance dominated electrical transport in the compressed nanowire. The reduced dimension and increased pressure should further contribute to the enhancement. At $P \approx P_{th}$, the grains started to merge together and nearly continuous conduction paths developed without any hindrances due to carbon matrix. With increasing pressure, for $P > P_{th}$, the grains overlapped and the amount of conducting path increased to form a continuum. The grains were hard to distinguished and it was much easier and straightforward for the current to find more shortest path resulting high conductivity at higher pressures. Figure 6 shows the increase of the conducting area $A_C$ by decreasing the isolated distinguishable grains in a single frame correlates the highly interconnected nature of electrical conductivity with microstructural evolution under high pressure.

## 4 Conclusion

Our paper extensively investigates the electrical transport properties of a single metal-carbon composite nanowire showing high sensitivity to external pressure stimulus at room temperature. The discussion further focused on the strong correlation between the percolation (macroscopic) and tunneling (quantum) phenomenon in the highly compressed nanowire. Strong nonlinear resistive responses were fully captured by studying the platinum grain coalescence process

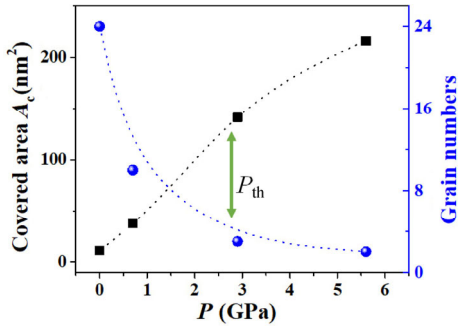


**Figure 6** The dependence of covered area $A_c$ that is covered by the current carrying conducting fillers as a function of pressure estimated from simulation. The distinguishable grain numbers decrease with pressure. The sharp changes in $A_c$ and grain numbers are clear around $P \approx P_{th}$.

and the formation of a conducting network. Such a mechanosensitive response might be applicable to a wide range of nanostructured devices to study the dynamics of promising new materials for nanoscale sensors, nanocapacitors, and resistive-memory (ReRAM) devices.

## Acknowledgements

This work was mainly supported by the National Natural Science Foundation of China (No. 11874076), the National Science Associated Funding (NSAF) (No. U1530402), and Science Challenging Program (No. TZ2016001). S. S. would also like to thank Dr. Christophe Thissieu from Almax easyLab Inc, MA, Cambridge, USA for providing the designer diamond anvils for the experiments. S. S. would like to thank Dr. Ankita Ghatak, S. N. Bose National Centre for Basic Sciences, Kolkata, India for the analysis and discussion on HRTEM data.

**Electronic Supplementary Material**: Supplementary material (further details of the nanowire growth process parameters and EDAX procedures, percolation model fitting, Voronoi network simulation, and TEM sample preparation) is available in the online version of this article at https://doi.org/ 10.1007/s12274-019-2295-x.

## References

[1] Xiao, X.; Yuan, L. Y.; Zhong, J. W.; Ding, T. P.; Liu, Y.; Cai, Z. X.; Rong, Y. G.; Han, H. W.; Zhou, J.; Wang, Z. L. High-strain sensors based on ZnO nanowire/polystyrene hybridized flexible films. *Adv. Mater.* **2011**, *23*, 5440–5444.

[2] Yamada, T.; Hayamizu, Y.; Yamamoto, Y.; Yomogida, Y.; Izadi-Najafabadi, A.; Futaba, D. N.; Hata, K. A stretchable carbon nanotube strain sensor for human-motion detection. *Nat. Nanotechnol.* **2011**, *6*, 296–301.

[3] Cai, J. Z.; Lu, L.; Kong, W. J.; Zhu, H. W.; Zhang, C.; Wei, B. Q.; Wu, D. H.; Liu, F. Pressure-induced transition in magnetoresistance of single-walled carbon nanotubes. *Phys. Rev. Lett.* **2006**, *97*, 026402.

[4] Cohen, D. J.; Mitra, D.; Peterson, K.; Maharbiz, M. M. A highly elastic, capacitive strain gauge based on percolating nanotube networks. *Nano Lett.* **2012**, *12*, 1821–1825.

[5] Ozden, S.; Autreto, P. A. S.; Tiwary, C. S.; Khatiwada, S.; Machado, L.; Galvao, D. S.; Vajtai, R.; Barrera, E. V.; Ajayan, M. P. Unzipping carbon nanotubes at high impact. *Nano Lett.* **2014**, *14*, 4131–4137.

[6] Pang, C.; Lee, G. Y.; Kim, T. I.; Kim, S. M.; Kim, H. N.; Ahn, S. H.; Suh, K. Y. A flexible and highly sensitive strain-gauge sensor using reversible interlocking of nanofibres. *Nat. Mater.* **2012**, *11*, 795–801.

[7] Gong, S.; Schwalb, W.; Wang, Y. W.; Chen, Y.; Tang, Y.; Si, J.; Shirinzadeh, B.; Cheng, W. L. A wearable and highly sensitive pressure sensor with ultrathin gold nanowires. *Nat. Commun.* **2014**, *5*, 3132.

[8] Kim, K. K.; Hong, S.; Cho, H. M.; Lee, J.; Suh, Y. D.; Ham, J.; Ko, S. H. Highly sensitive and stretchable multidimensional strain sensor with prestrained anisotropic metal nanowire percolation networks. *Nano Lett.* **2015**, *15*, 5240–5247.

[9] Park, J.; Lee, Y.; Hong, J.; Ha, M.; Jung, Y. D.; Lim, H.; Kim, S. Y.; Ko, H. Giant tunneling piezoresistance of composite elastomers with interlocked microdome arrays for ultrasensitive and multimodal electronic skins. *ACS Nano* **2014**, *8*, 4689–4697.

[10] Jibril, L.; Ramírez, J.; Zaretski, A. V.; Lipomi, D. J. Single-nanowire strain sensors fabricated by nanoskiving. *Sens. Actuators A Phys.* **2017**, *263*, 702–706.

[11] Jeon, J.; Lee, H. B. R.; Bao, Z. N. Flexible wireless temperature sensors based on Ni microparticle-filled binary polymer composites. *Adv. Mater.* **2013**, *25*, 850–855.

[12] Chen, Z.; Pfattner, R.; Bao, Z. N. Characterization and understanding of thermoresponsive polymer composites based on spiky nanostructured fillers. *Adv. Electron. Mater.* **2017**, *3*, 1600397.

[13] Bartlett, M. D.; Kazem, N.; Powell-Palm, M. J.; Huang, X. N.; Sun, W. H.; Malen, J. A.; Majidi, C. High thermal conductivity in soft elastomers with elongated liquid metal inclusions. *Proc. Natl. Acad. Sci. USA* **2017**, *114*, 2143–2148.

[14] Paul, R.; Dai, L. M. Interfacial aspects of carbon composites. *Compos. Int.* **2018**, *25*, 539–605.

[15] Zaretski, A. V.; Root, S. E.; Savchenko, A.; Molokanova, E.; Printz, A. D.; Jibril, L.; Arya, G.; Mercola, M.; Lipomi, D. J. Metallic nanoislands on graphene as highly sensitive transducers of mechanical, biological, and optical signals. *Nano Lett.* **2016**, *16*, 1375–1380.

[16] Mikheykin, A. S.; Dmitriev, V. P.; Chagovets, S. V.; Kuriganova, A. B.; Smirnova, N. V.; Leontyev, I. N. The compressibility of nanocrystalline Pt. *Appl. Phys. Lett.* **2012**, *101*, 173111.

[17] Yang, X.; Hu, J.; Chen, S. M.; He, J. L. Understanding the percolation characteristics of nonlinear composite dielectrics. *Sci. Rep.* **2016**, *6*, 30597.

[18] Fostner, S.; Brown, R.; Carr, J.; Brown, S. A. Continuum percolation with tunneling. *Phys. Rev. B* **2014**, *89*, 075402.

[19] Balberg, I. Tunneling and nonuniversal conductivity in composite materials. *Phys. Rev. Lett.* **1987**, *59*, 1305–1308.

[20] Toker, D.; Azulay, D.; Shimoni, N.; Balberg, I.; Millo, O. Tunneling and percolation in metal-insulator composite materials. *Phys. Rev. B* **2003**, *68*, 041403.

[21] Schwalb, C. H.; Grimm, C.; Baranowski, M.; Sachser, R.; Porrati, F.; Reith, H.; Das, P.; Müller, J.; Völklein, F.; Kaya, A. et al. A tunable strain sensor using nanogranular metals. *Sensors* **2010**, *10*, 9847–9856.

[22] Park, J. H.; Steingart, D. A.; Kodambaka, S.; Ross, F. M. Electrochemical electron beam lithography: Write, read, and erase metallic nanocrystals on demand. *Sci. Adv.* **2017**, *3*, e1700234.

[23] Córdoba, R.; Ibarra, A.; Mailly, D.; Ma De Teresa, J. Vertical growth of superconducting crystalline hollow nanowires by $He^+$ focused ion beam induced deposition. *Nano Lett.* **2018**, *18*, 1379–1386.

[24] Fernández-Pacheco, A.; De Teresa, J. M.; Córdoba, R.; Ibarra, M. R. Metal-insulator transition in Pt-C nanowires grown by focused-ion-beam-induced deposition. *Phys. Rev. B* **2009**, *79*, 174209.

[25] Beloborodov, I. S.; Efetov, K. B.; Lopatin, A. V.; Vinokur, V. M. Transport properties of granular metals at low temperatures. *Phys. Rev. Lett.* **2003**, *91*, 246801.

[26] Liao, Z. M.; Xu, J.; Zhang, X. Z.; Yu, D. P. The relationship between quantum transport and microstructure evolution in carbon-sheathed Pt granular metal nanowires. *Nanotechnology* **2008**, *19*, 305402.

[27] Beloborodov, I. S.; Lopatin, A. V.; Vinokur, V. M.; Efetov, K. B. Granular electronic systems. *Rev. Mod. Phys.* **2007**, *79*, 469–518.

[28] Kolb, F.; Schmoltner, K.; Huth, M.; Hohenau, A.; Krenn, J.; Klug, A.; List, E. J. W.; Plank, H. Variable tunneling barriers in FEBID based PtC metal-matrix nanocomposites as a transducing element for humidity sensing. *Nanotechnology* **2013**, *24*, 305501.

[29] Durkan, C.; Welland, M. E. Size effects in the electrical resistivity of polycrystalline nanowires. *Phys. Rev. B* **2000**, *61*, 14215–14218.

[30] Prasad Manoharan, M.; Kumar, S.; Haque, M. A.; Rajagopalan, R.; Foley, H. C. Room temperature amorphous to nanocrystalline transformation in ultra-thin films under tensile stress: An *in situ* TEM study. *Nanotechnology* **2010**, *21*, 505707.

[31] Zhu, J.; Quan, Z.; Wang, C.; Wen, X.; Jiang, Y.; Fang, J.; Wang, Z.; Zhao, Y.; Xu, H. Structural evolution and mechanical behaviour of Pt nanoparticle superlattices at high pressure. *Nanoscale* **2016**, *8*, 5214–5218.

[32] Liao, H. G.; Cui, L. K.; Whitelam, S.; Zheng, H. M. Real-time imaging of $Pt_3Fe$ nanorod growth in solution. *Science* **2012**, *336*, 1011–1014.

[33] http://www.almax-easylab.com/WebsitePatternedAnvils01.aspx. **[Dear author, please complete this ref.,thanks]**

[34] Kiuchi, M.; Matsui, S.; Isono, Y. The piezoresistance effect of FIB-deposited carbon nanowires under severe strain. *J. Micromech. Microeng.* **2008**, *18*, 065011.

[35] Chakravorty, M.; Das, K.; Raychaudhuri, A. K.; Naik, J. P.; Prewett, P. D. Temperature dependent resistivity of platinum–carbon composite nanowires grown by focused ion beam on $SiO_2$/Si substrate. *Microelectron. Eng.* **2011**, *88*, 3360–3364.

[36] Faraby, H.; DiBattista, M.; Bandaru, P. R. Percolation of gallium dominates the electrical resistance of focused ion beam deposited metals. *Appl. Phys. Lett.* **2014**, *104*, 173107.

[37] Barzola-Quiquia, J.; Schulze, S.; Esquinazi, P. Transport properties and atomic structure of ion-beam-deposited W, Pd and Pt nanostructures. *Nanotechnology* **2009**, *20*, 165704.

[38] Lin, J. F.; Bird, J. P.; Rotkina, L.; Bennett, P. A. Classical and quantum transport in focused-ion-beam-deposited Pt nanointerconnects. *Appl. Phys. Lett.* **2003**, *82*, 802–804.

[39] Peñate-Quesada, L.; Mitra, J.; Dawson, P. Non-linear electronic transport in Pt nanowires deposited by focused ion beam. *Nanotechnology* **2007**, *18*, 215203.

[40] He, R. R.; Yang, P. D. Giant piezoresistance effect in silicon nanowires. *Nat. Nanotechnol.* **2006**, *1*, 42–46.

[41] De Teresa, J. M.; Córdoba, R.; Fernández-Pacheco, A.; Montero, O.; Strichovanec, P.; Ibarra, M. R. Origin of the difference in the resistivity of as-grown focused-ion- and focused-electron-beam-induced Pt nanodeposits. *J. Nanomater.* **2009**, *2009*, 936863.

[42] Vaz, A. R.; da Silva, M. M.; Leon, J.; Moshkalev, S. A.; Swart, J. W. Platinum thin films deposited on silicon oxide by focused ion beam: Characterization and application. *J. Mater. Sci.* **2008**, *43*, 3429–3434.

[43] Lin, J. F.; Bird, J. P.; Rotkina, L.; Sergeev, A.; Mitin, V. Large effects due to electron–phonon-impurity interference in the resistivity of Pt/C-Ga composite nanowires. *Appl. Phys. Lett.* **2004**, *84*, 3828–3830.

[44] Wei, Y. X.; Wang, R. J.; Wang, W. H. Soft phonons and phase transition in amorphous carbon. *Phys. Rev. B* **2005**, *72*, 012203.

[45] Hoppel, C. P. R.; Bogetti, T. A.; Gillespie, J. W. Jr. Literature review-effects of hydrostatic pressure on the mechanical behavior of composite materials. *J. Thermoplast. Compos. Mater.* **1995**, *8*, 375–409.

[46] Bousige, C.; Balima, F.; Machon, D.; Pinheiro, G. S.; Torres-Dias, A.; Nicolle, J.; Kalita, D.; Bendiab, N.; Marty, L.; Bouchiat, V. et al. Biaxial strain transfer in supported graphene. *Nano Lett.* **2017**, *17*, 21–27.

[47] Rotundu, C. R.; Ćuk, T.; Greene, R. L.; Shen, Z. X.; Hemley, R. J.; Struzhkin, V. V. High-pressure resistivity technique for quasi-hydrostatic compression experiments. *Rev. Sci. Instrum.* **2013**, *84*, 063903.

[48] Sun, L.; Wu, Q. Pressure-induced exotic states in rare earth hexaborides. *Rep. Prog. Phys.* **2016**, *79*, 084503.

[49] Dukic, M.; Winhold, M.; Schwalb, C. H.; Adams, J. D.; Stavrov, V.; Huth, M.; Fantner, G. E. Direct-write nanoscale printing of nanogranular tunnelling strain sensors for sub-micrometre cantilevers. *Nat. Commun.* **2016**, *7*, 12487.

[50] Lau, D. W.; McCulloch, D. G.; Taylor, M. B.; Partridge, J. G.; McKenzie, D. R.; Marks, N. A.; Teo, E. H. T.; Tay, B. K. Abrupt stress induced transformation in amorphous carbon films with a highly conductive transition phase. *Phys. Rev. Lett.* **2008**, *100*, 176101.

[51] Nishi, Y.; Hirano, M. Bending stress dependent electrical resistivity of carbon fiber in polymer for health monitoring system. *Mater. Trans.* **2007**, *48*, 2735–2738.

[52] Li, X. Y.; Mao, H. K. Solid carbon at high pressure: Electrical resistivity and phase transition. *Phys. Chem. Miner.* **1994**, *21*, 1–5.

[53] Sagar, R. U. R.; Zhang, X. Z.; Xiong, C. Y.; Yu, Y. Semiconducting amorphous carbon thin films for transparent conducting electrodes. *Carbon* **2014**, *76*, 64–70.

[54] Chang, K. C.; Odagaki, T. Localization and tunneling effects in percolating systems. *Phys. Rev. B* **1987**, *35*, 2598–2603.

[55] Huth, M.; Porrati, F.; Schwalb, C.; Winhold, M.; Sachser, R.; Dukic, M.; Adams, J.; Fantner, G. Focused electron beam induced deposition: A perspective. *Beilstein J. Nanotechnol.* **2012**, *3*, 597–619.

[56] Agraït, N.; Yeyati A. L.; van Ruitenbeek, J. M. Quantum properties of atomic-sized conductors. *Phys. Rep.* **2003**, *377*, 81–279.

[57] Nenashev, A. V.; Jansson, F.; Baranovskii, S. D.; Österbacka, R.; Dvurechenskii, A. V.; Gebhard, F. Hopping conduction in strong electric fields: Negative differential conductivity. *Phys. Rev. B* **2008**, *78*, 165207.

[58] Park, C. H.; Lee, S. Y.; Hwang, D. S.; Shin, D. W.; Cho, D. H.; Lee, K. H.; Kim, T. W.; Kim, T. W.; Lee, M.; Kim, D. S. et al. Nanocrack-regulated self-humidifying membranes. *Nature* **2016**, *532*, 480–483.